Oinam *et al. Int J Concr Struct Mater* (2022) 16:62
https://doi.org/10.1186/s40069-022-00551-7

International Journal of Concrete Structures and Materials

RESEARCH Open Access

Characteristics of GGBFS-Based Pervious Concrete Considering Rheological Properties of the Binder

Yanchen Oinam[1], Suhawn Ju[1], Seongwoo Gwon[2], Myoungsu Shin[1*] and Sukhoon Pyo[1*]

Abstract

To mitigate environmental challenges, such as urban flooding, noise pollution, and the urban heat island effect, pervious concrete has been developed. This research was intended to develop pervious concrete made from ground granulated blast furnace slag (GGBFS) to further decrease the environmental impact of the construction sector by reducing the content of ordinary Portland cement (OPC). The primary objective of the mix proportion was to maximize water permeability while meeting the required compressive strength. Two levels (60 and 100%) of OPC replacement by GGBFS were evaluated and compared to OPC-only concrete, and two target porosities (10 and 15%) were achieved by modifying the binder-to-aggregate ratio. CaO and $CaCl_2$ were utilized as an activator and an accelerator, respectively, for the GGBFS only binder. Characteristics of the pervious concrete were determined with the compressive strength, porosity and water permeability test. Meanwhile, the effects of the rheological properties of binders on the water permeability and compressive strength of pervious concretes was evaluated. According to the results, the permeability of pervious concretes always exhibited a positive correlation with porosity, regardless of binder type. Although, the pervious concrete made with CaO-activated GGBFS has a lower compressive strength than the other two cases (60% GGBFS and only OPC), it still meets the minimum strength requirement. Based on the rheology studies of binder, it was found that, the adhesion force of the binder and the compressive strength of the pervious concrete decreases, as evaluated by rheology studies on binders. The CT scan revealed that when the adhesive force of the binder was weaker, the local porosity was higher (i.e., pore volume was larger) at the bottom of the specimen, which might be due to the limited consolidation and compaction of the binder between aggregate particles at the bottom due to its higher plastic viscosity.

Keywords: adhesion, water permeability, porosity, CaO activated GGBFS, CT scan

1 Introduction

Groundwater contamination, noise pollution, and the urban heat island effect are representative examples of the environmental contamination caused by the significant devastation of the environment (Thompson et al., 2022; Yao et al., 2022; Zhang et al., 2022). Meanwhile, it is known that pervious concrete (also known as porous concrete) is a feasible approach for addressing such environmental difficulties using it in pavement construction (Cui et al., 2017; da Costa et al., 2021; Kim et al., 2018; Lin et al., 2016; Liu et al., 2020; Lu et al., 2019). Pervious concrete is manufactured with less binder, so the pores are interconnected and water can pass through it (Huang et al., 2010; Kim et al., 2016; Peng et al., 2018). It typically consists of coarse aggregate and cementitious binder, with very little to no fine aggregate. The nominal

Journal information: ISSN 1976-0485/eISSN2234-1315.

*Correspondence: msshin@unist.ac.kr; shpyo@unist.ac.kr

[1] Department of Urban and Environmental Engineering, Ulsan National Institute of Science and Technology (UNIST), 50 UNIST-gil, Ulsan 44919, Republic of Korea
Full list of author information is available at the end of the article

aggregate size commonly utilized to make pervious concrete is between 10 and 20 mm (Yu et al., 2019).

For better knowledge of the properties of pervious concrete, the mix design should consider a variety of factors, such as aggregate size, aggregate type, supplementary cementitious materials (SCMs), and binder ingredients. According to (Sriravindrarajah et al., 2012), the aggregate size has a substantial impact on the porosity and compressive strength of pervious concrete, and there is no effect of the aggregate type on the correlation between porosity and permeability. Lee et al. (2016) found that porosity slightly increases with ground granulated blast furnace slag (GGBFS) and fly ash-based pervious concrete compared with ordinary Portland cement (OPC)-based pervious concrete, but it was also observed that the compressive strength of the GGBFS and fly ash-based pervious concrete decreases slightly. Meanwhile, Saboo et al. (2019) suggested that using SCMs as a partial replacement can improve workability and compressive strength using less OPC in pervious concrete.

It should also be considered that the workability and rheological properties of the binder play a critical role in determining the compressive strength of pervious concrete. Even though the Bingham model is generally applied to represent the rheological properties of cementitious materials, Wang and Liu (2020) reported that Casson and Herschel–Bulkley models could also be compatible with the flow behaviors of certain mixtures. The fresh paste tends to be stiffened when the amount of solid content increases, which leads to a higher viscosity and dynamic yield stress (Wang et al., 2018). Meanwhile, Park et al. (2022) recently revealed that the adhesive force of the binder correlates with the compressive strength of concrete, and the flow of the binder affects the compressive strength of pervious concrete. When the flowability was not appropriate (either low or high), the binder was not uniformly distributed over the thickness of the specimen, which resulted in the segregation of the binder and aggregate (da Costa et al., 2021; Park et al., 2022). The flowability has a strong relation to adhesion properties between the binder and coarse aggregate; a low flowability caused the presence of more binder at the top portion of the specimen (da Costa et al., 2021), while a high flowability resulted in the settlement of more binder to the bottom (Park et al., 2022).

The water permeability of pervious concrete depends on the size and distribution of the pores, which is usually measured with the constant head or falling head test methods. The applications of these test methods vary regarding equipment and analysis, depending on standards and specifications (EN 12697-19; ASTM C1701). The permeability coefficient is determined by the operating technique and the results of water permeability are not uniform (Batezini & Balbo, 2015; Zhang et al., 2020). In addition, with the usage of either the head or the hydraulic gradient, the calculated permeability may change (Qin et al., 2015). Previously, a study was conducted for the falling head test method with disparate head levels, and it was suggested that the use of a higher head level provides a better correlation between porosity and water permeability (Chandrappa & Biligiri, 2016). Despite the availability of these three test methods, no study has been undertaken to compare and select a more convenient and reliable water permeability test method for pervious concrete.

The cement industry produces an enormous amount of greenhouse gases, which are estimated at around 6–8% of global emissions (Naik, 2005). It is generally known that the utilization of GGBFS could be a practical solution to reduce environmental impacts, since it is an industrial byproduct, and the use of GGBFS as a partial replacement can improve the various properties of concrete, although its early strength may decrease (Meyer, 2009; Song & Saraswathy, 2006). GGBFS is normally activated using alkali activators, such as sodium hydroxide (NaOH) and sodium silicates. However, calcium oxide (CaO) and calcium hydroxide ($Ca(OH)_2$) were used as alternatives to alkali activators following Kim et al. (2013). The addition of accelerators such as calcium bicarbonate, calcium chloride ($CaCl_2$), calcium formate and even aluminium sulfate at a certain dosage may reduce the initial setting time and increase the initial heat of hydration of cementitious materials (Wang,et al., 2019a, 2019b; Yum et al., 2017, 2020). Moreover, no attempt has been made to investigate the effect of the rheological properties of CaO-activated GGBFS on pervious concrete.

Given the research need, in this paper, thorough research has been conducted to study the importance of pervious concrete manufactured using GGBFS and OPC. For this research, the flowability of the binder, compressive strength, porosity, and water permeability of the pervious concrete were studied for a fair comparison with the distinct mix designs. Due to the exclusion of fine aggregate and less binder in pervious concrete, the flowability cannot determine the characteristics of the mix design. To address this, the significant effect of the rheological properties of the binders on GGBFS based pervious concrete was examined. A computed tomography (CT) scan test was also conducted to compare the porosity measured by the conventional porosity test method and to analyze the distribution of pores associated with the rheological properties throughout the structure of the pervious concrete.

2 Materials and Specimen Preparation

2.1 Materials

The binder materials used for this study were Type I OPC and GGBFS as shown in Fig. 1a, b, respectively, and the chemical compositions of the raw materials are listed in Table 1. CaO and $CaCl_2$ were used as an activator and accelerator for the fabrication of GGBFS binder and concrete, manufactured by Daejung Chemicals (Korea) as shown in Fig. 1c, d with a density of 3.3–3.4 and 2.16 g/$cm^{3,}$ respectively. The flow of the binder was controlled using polycarboxylate-based liquid superplasticizer (SP) manufactured by Sika Korea. The size of natural coarse aggregate used ranged 9–13 mm, and no fine aggregate was used.

Table 1 Chemical oxide compositions of raw materials.

Oxide	OPC (wt.%)	GGBFS (wt.%)
CaO	64.48	46.22
SiO_2	19.38	33.14
Al_2O_3	4.48	13.4
MgO	2.82	3.09
SO_3	3.305	1.93
K_2O	1.08	0.474
Fe_2O_3	3.455	0.427
Na_2O	0.16	0.204

2.2 Mix Design

The mix proportions of the pervious concretes tested in this study are shown in Table 2. The primary objective of the mix proportion was to maximize water permeability while meeting the required compressive strength (ACI. 2010). A total of six mix designs were prepared: two for each of three binder types: 100% OPC (C100), 40% OPC and 60% GGBFS (C40G60), and 100% GGBFS (G100). To achieve the target porosity, the bulk porosity of aggregate was measured and binder was allowed to fill the pores by subtracting the desirable porosity (Park et al., 2022). The two mix proportions for each binder were designed to have two target porosities of 10% (P10)

Fig. 1 **a** OPC; **b** GGBFS; **c** CaO and **d** $CaCl_2$

Table 2 Mix proportions of the tested pervious concretes.

Name	Target porosity (%)	*w/b* ratio	Weight of the material (kg/m^3)						
			Aggregate	OPC	Water	GGBFS	$CaCl_2$	CaO	SP
G100P10	10	0.3	1546	–	151	444	10.1	49.4	0.25
G100P15	15	0.3	1546	–	127	375	8.5	41.7	0.21
C40G60P10	10	0.3	1546	204	153	306	–	–	1.02
C40G60P15	15	0.3	1546	172	129	259	–	–	0.86
C100P10	10	0.3	1546	523	157	–	–	–	1.04
C100P15	15	0.3	1546	443	133	–	–	–	0.88

Table 3 Flow test results of fresh binders with different amounts of superplasticizer.

SP (wt.%)	Flow (mm)		
	G100 (*w/b* = 0.3)	C40G60 (*w/b* = 0.3)	C100 (*w/b* = 0.3)
0	190	163	191
0.05	210	–	–
0.1	265	175	204
0.15	300 + (overflow)	–	–
0.2	–	214	213
0.3	–	272	239

and 15% (P15) to study the effect of adhesion force with larger volume of binder and to attain a higher strength pervious concrete. CaO and $CaCl_2$ were employed as an activator and accelerator, respectively, for G100, and their amounts were determined based on the preliminary examination to achieve a similar strength of recent study (Yum et al., 2017). They reported that the use of $CaCl_2$ can increase the consumption of Ca $(OH)_2$, thus increase the strength. It was also revealed that the incorporation of $CaCl_2$ resulted in the formation of hydrotatlcite and strätlingite while accelerating the dissolution of glass phase of GGBFS and fly ash in the early days (Yum et al., 2017). SP was added to control the flowability of the tested binders at a similar level. Nine cylindrical samples of 100 × 200 mm were fabricated at one batch for each mixture type. Among them, three samples each were tested for compressive strength at 7 and 28 days of curing, respectively. The rest three samples were used to measure porosity and water permeability, and one of the three samples was scanned by computer tomography. The water/binder (w/b) ratio in all the mix designs was fixed at 0.30.

A flow table test of the binders was conducted following ASTM C230 (2020) to determine the amount of SP in each mixture that can allow a similar flowability among the tested mixtures. Table 3 depicts the flow test results of the binders with different amounts of SP, which was added by the weight percent of the binder. A medium flow of approximately 210–220 mm is deemed suitable according to (Park et al., 2022) and was selected for this study. In the case of G100, the addition of 0.05% SP gave a medium flow of 210 mm. On the other hand, for the binders C100 and C40G60, the use of 0.2% SP achieved a flow of 213 and 214 mm, respectively. Therefore, the amount of SP in each mixture in Table 2 was determined based on the results of the flow test.

2.3 Sample Fabrication

The preparation of all specimens followed the same procedures. First, all the powder materials, including the activator (if any), were dry mixed separately in a planetary mixer for 5 min. Water and superplasticizer were added and mixed for an additional 5 min. Subsequently, the binder was again further mixed with the coarse aggregate on a concrete drum mixer until it was observed to be blended properly. The resulting concrete was poured on cylindrical molds of 100 × 200 mm. Two layers were filled in and compacted with 100 blows of rodding. The samples cast were cured in a sealed condition with polyethylene foil at a room temperature (20–25 °C) and relative humidity of 60 ± 5% and demolded from the molds after 24 h. The samples were then demolded and placed in a water bath during the specified periods (7 and 28 days of curing). The binder paste was cast into cube molds with a side of 50 mm and subjected to the same preparation procedures for curing until testing.

3 Testing Methods

3.1 Rheology

A rheology test of the binders was conducted using a commercial rheometer (HAAKE MARS III, Thermo Fisher Scientific, USA) as shown in Fig. 2 to determine the yield stress, viscosity, and adhesion force of the binder. Three binders used for conducting the rheology test were C100, C40G60 and G100 with flow range from 210 to 214 mm. It was prepared following the same

Fig. 2 Rheometer (HAAKE MARS III).

procedure as discussed in Sect. 2.3. The fresh binder was placed between two parallel plates with a diameter of 60 mm, and the gap was set to be 2 mm between the upper and lower plates. When the subjected initial gap touched the sample, the extra materials on the edge were removed. If the shearing surfaces are smooth, slippage can occur (Park et al., 2022). To avoid slipping between the binder and the plates, sandpaper was attached onto the plates.

The employed shearing protocol for the rheology test is portrayed in Fig. 3. The shear strain rate was gradually increased until it reached 60 s^{-1} for up to 30 s. The pre-shear rate of 60 s^{-1} was determined from the preliminary test, in which the measured data were consistent, and it was maintained for 90 s to allow stress relaxation (Ma et al., 2018). The stepwise reduction of the shear rate was the principle behind measuring shear stress, and each step was measured for 15 s and one data was collected per second (Gwon & Shin, 2019). The Bingham model was employed to measure the yield stress and plastic viscosity, because the binders utilized in this investigation are Bingham plastic fluids (Gołaszewski & Szwabowski, 2004; ASTM C, 1749 17A, 2012; Wang et al., 2020).

The binder's adhesive force was determined by allowing the upper plate to move at a constant pace. The force exerted by the upper plate was measured until it was negligible. An example of a measured adhesive force is revealed in Fig. 4. It shows the behavior of the binder's adhesive force initially at a closer gap and increase of the gap gradually between the two plates over a duration. The highest adhesive force measured during each test was compared.

3.2 Compressive Strength

Pervious concrete and hardened binders were tested for compressive strength in accordance with ASTM C, 1231, (2015) and ASTM C109, (2020), respectively. For the pervious concrete, each three cylindrical samples of size 100 × 200 mm from the six mixtures which were cured for 7 and 28 days were subjected for the compressive strength test. Meanwhile, each three cube samples of 50 mm which were also cured for 7 and 28 days from the three mixtures of binder of C100, C40G60 and G100 were used for compressive strength test of the hardened binder.

3.3 Porosity

The total porosity of the pervious concrete specimens was determined following Archimedes' principle (Alemu et al., 2021; Kim et al., 2018). From each mixture, three cylindrical samples of 100 × 200 mm were used for conducting the porosity test. The weight of the samples in underwater and dried conditions was measured to calculate the total porosity of the pervious concrete using Eq. (1) (Alemu et al., 2021; Kim et al., 2018) The samples were dried at a temperature of 60 °C for 24 h to avoid changes in crystal structure and cracks within the specimen due to high temperature (Sun et al., 2018):

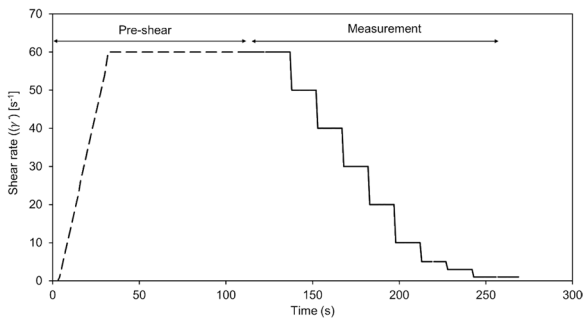

Fig. 3 Shearing protocol for the rheology test.

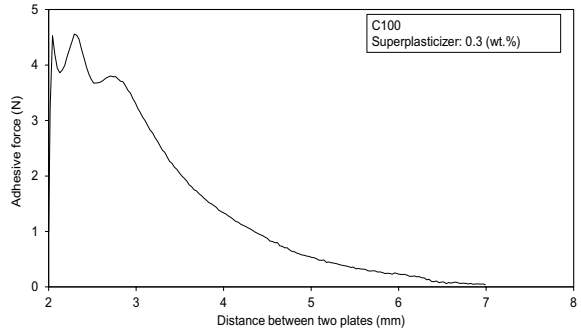

Fig. 4 Example of adhesive force measurement.

$$P = \left[1 - \left(\frac{M_d - M_s}{\rho_w \times v}\right)\right] \times 100\# \quad (1)$$

where P is the total porosity (%), M_d is the dry weight of the sample (g), M_s is the submerged weight of the sample (g), v is the volume of the sample (mm^3), and ρ_w is the density of water (g/mm^3) at 20–23 °C.

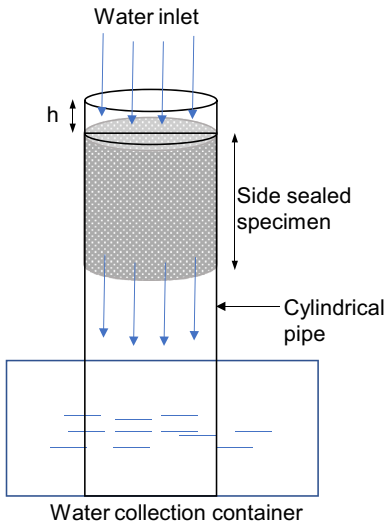

Fig. 5 Schematic of the constant head test method (ASTM C1701).

3.4 Water Permeability

In this study, water permeability test was conducted following three methods using the three replicate samples of each mix to obtain the average permeability measurement for a fair comparison. Three water permeability test methods were adopted, since there are few objective analysis of water permeability test methods.

The water permeability of the samples was measured using the following three test methods: (i) The constant head test method, which follows ASTM C 1701, (2017), as shown in Fig. 5; (ii) The constant head test method measuring vertical and horizontal permeability using EN 12697-19 (2012), as shown in Fig. 6; and (iii) the falling head test (Batezini & Balbo, 2015) method, as depicted in Fig. 7. Notably, ASTM C1701 is generally used for the application of determining the water infiltration rate of in situ pervious pavement. Meanwhile, the EN test method is known for determining the vertical and horizontal water permeability of bituminous mixtures of interconnecting voids. Regardless of the application of the two water permeability test methods, both standard methods followed the similar principle of the constant head test method.

The samples were sealed with polyethylene foil and duct tape to avoid the leakage of water from the sides, except for the samples tested for horizontal permeability following EN 12697-19. All specimens were previously saturated before any of the actual permeability tests were conducted to fill the pores of the specimen

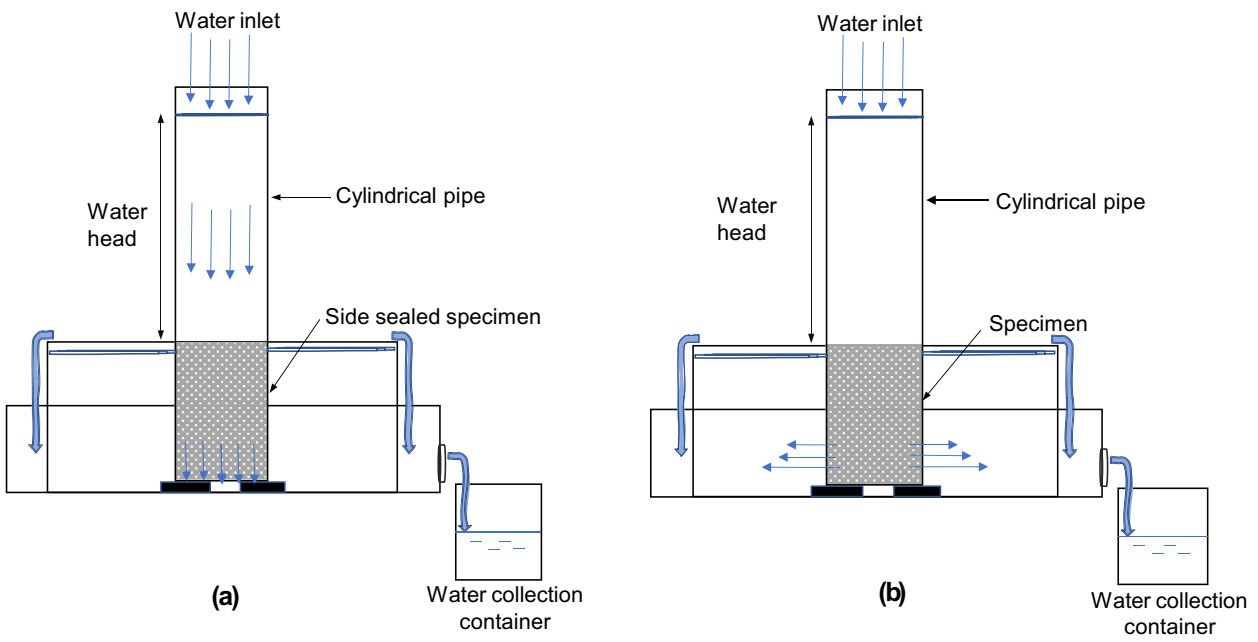

Fig. 6 Schematic of the constant head test method: **a** vertical; and **b** horizontal (EN 12697-19).

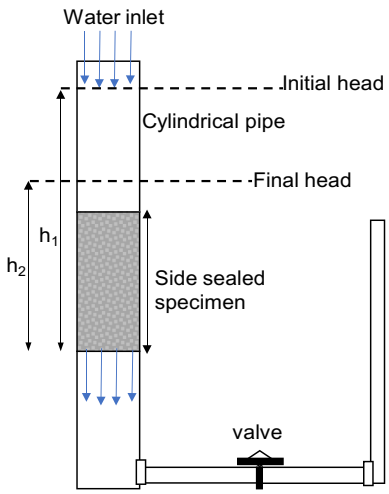

Fig. 7 Schematic of the falling head test method (Batezini & Balbo, 2015).

(Chandrappa & Biligiri, 2016). Equations 2 (ASTM C1701, 2017), 3 (EN 12697-19, 2012), 4 (EN 12697-19, 2012), and 5 (Batezini & Balbo, 2015) represent the formulas for the ASTM, EN vertical, EN horizontal, and falling head test methods, respectively:

$$I = \frac{KM}{D^2 \times t_c} \tag{2}$$

$$k_{\mathrm{f,v}} = \frac{(4 \times Q_{\mathrm{v}} \times l)}{h\pi D^2} \tag{3}$$

$$k_{\mathrm{f,h}} = \frac{Q_{\mathrm{v}}}{h \times \pi D} \tag{4}$$

$$k_f = \left(\frac{a \times l}{A \times t_f}\right) l n \frac{h_1}{h_2} \tag{5}$$

where I is the infiltration rate (mm/h), which is later calculated in terms of (mm/s). M is the mass of the infiltrated water (1.2 kg). D is the inside diameter of the infiltration ring (98 mm), and t_c is the time required for a measured amount of water to infiltrate the concrete(s). K is a constant; $k_{\mathrm{f,v}}$ and $k_{\mathrm{f,h}}$ are the vertical and horizontal water permeability coefficients, respectively, Q_{v} is the measured water flow through the specimen (m^3/s), l is the thickness of the specimen (200 mm), and h is the actual height of the water column (300 mm). D is the diameter of the specimen (100 mm), and k_{f} is the water permeability coefficient (falling head). Moreover, a (mm^2) and A (mm^2) are the cross sections of the tube and specimen, respectively, t_{f} is the time measured for the water to infiltrate, and h_1 (650 mm) and h_2 (250 mm) are the initial and final heads.

3.5 Computer Tomography

In this study, 3D CT scan measurements were conducted to measure the pore distribution of the pervious concrete with the help of cone-beam computed tomography (CS9300, Carestream Health Inc., Rochester, NY). Among the three specimens of water permeability and porosity tests, one specimen per mixture was subjected to a CT scan test. The voxel size was 0.3 mm, the voltage was 100 kVp, and the current was 30 mA (Alemu et al., 2021; Park et al., 2022). 3D contours of the specimens and axial images were captured during the process of CT scanning. By counting the pixels of the darker and brighter portions, which represent pores and skeletons, the porosity of the pervious concrete was calculated, as illustrated in Fig. 8. MATLAB was used to convert the raw CT images to binary images consisting of dark and brighter portion of the surface (Alemu et al., 2021). In addition, after determining the required region of interest, ImageJ was used to calculate the porosity image of the whole cross-sectional diameter (100 mm) by filtering out the noise included in the binary images. The process was applied for all the 409 raw CT scan pictures of each sample of the six mix designs of the pervious concrete. Furthermore, porosity characteristics along the height direction were obtained

4 Results and Discussion

4.1 Rheological Properties of the Binder

4.1.1 Viscosity and Yield Stress

Rheology tests of the binders were conducted to discern the viscosity and adhesive properties of the binder with respect to aggregate. Fig. 9 represents the shear stress–strain rate responses of the fresh binders. The coefficients (R^2) of determination of all the binders were quite acceptable, which denotes a good correlation between the shear stress and shear rate. During the test, it was observed that, with G100, the resistance to flow (i.e., plastic viscosity) was much higher than the others with less GGBFS, which resulted in higher friction force between the upper rheometer plate and the surface of the specimens.

Fig. 10 reveals that, among all the binders, G100 and C100 had the maximum viscosity of 5.8 Pa s and the lowest viscosity of 1.2 Pa s, respectively. The plastic viscosity increased as the percentage of GGBFS increased. Among the three mixtures, G100 displayed the highest plastic viscosity. The use of $CaCl_2$ as an accelerator can increase the initial setting time and the initial heat of hydration because of its activation with CaO, which produces a quick hardening of binder surface at which the plastic viscosity of G100 binder might increases (Yum et al., 2017). The increase in plastic viscosity may also be attributable to the structural breakdown of the G100

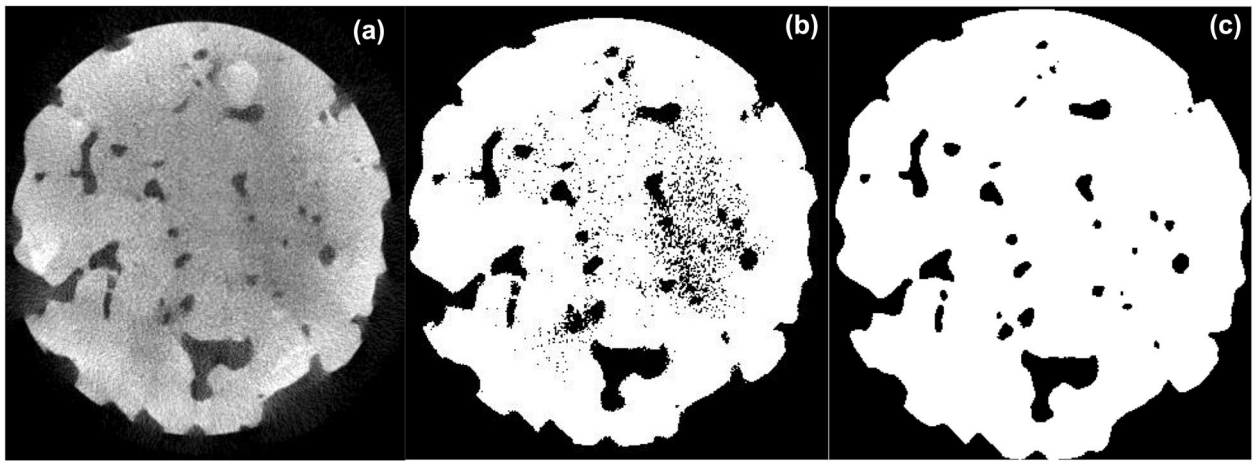

Fig. 8 Image processing **a** raw CT image; **b** binary image; and **c** filtered image.

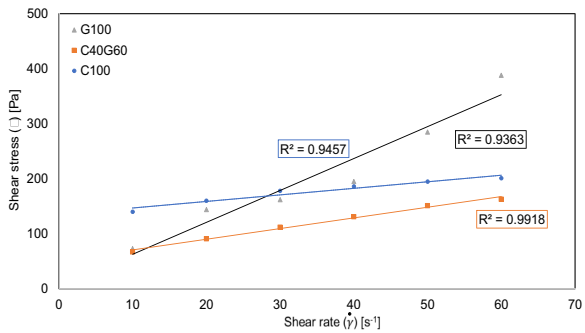

Fig. 9 Shear stress–strain rate responses of the binders.

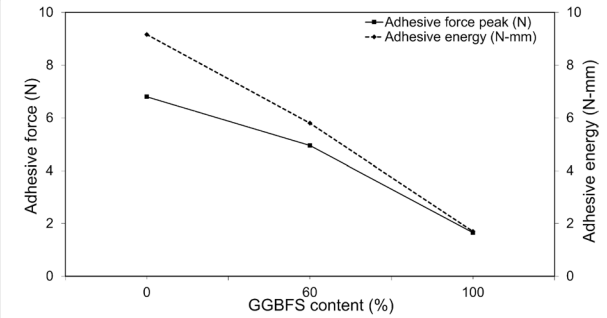

Fig. 11 Adhesive force and energy of the binders.

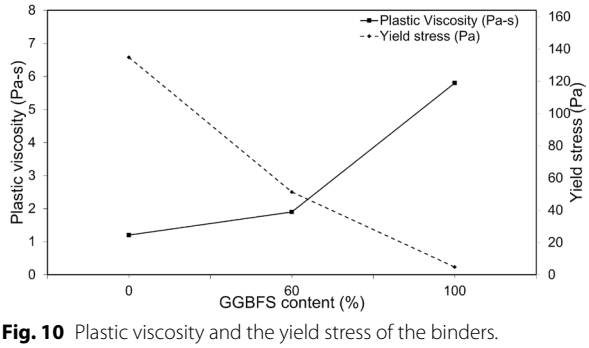

Fig. 10 Plastic viscosity and the yield stress of the binders.

binder caused by shear energy applied for the rheology test (Palacios et al., 2008).

As demonstrated in Fig. 10, the yield stress of the tested mixtures tended to decrease as the GGBFS content increased. C100 shows the greatest yield stress which may be attributable to improved adhesion between particles without paste segregation (Park et al., 2022). Likewise, the yield stress of G100 was lower than that of C100. Regardless of the yield stress or plastic viscosity of the binders, appropriate flowability is essential. This investigation also demonstrated that since a significant amount of coarse aggregate and a lesser content of binder was included in the mix design of pervious concrete, the rheological properties of binder such as yield stress and plastic viscosity could not significantly control the mechanical properties of the pervious concrete.

4.1.2 Adhesive Force

Fig. 11 illustrates the adhesive properties of the fresh binders according to the amount of GGBFS content in the fresh binders. When the GGBFS content was zero, the adhesive property was the highest. However, with the increase in the amount of GGBFS, the adhesive properties of the fresh binder decreases. The highest and lowest adhesive force was 6.8 and 1.65 N, respectively. The adhesive properties of the fresh binders had a significant effect on the compressive strength of the pervious concrete,

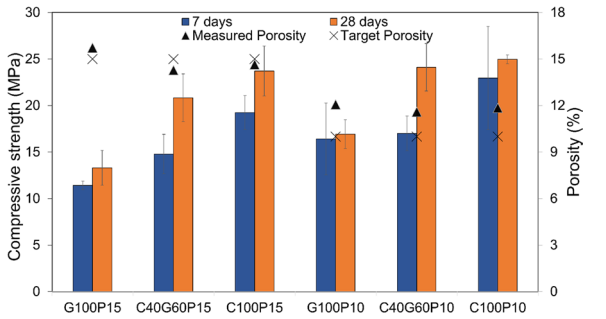

Fig. 12 Relationship between compressive strength (7 and 28 days) and porosity of the tested concrete mixtures.

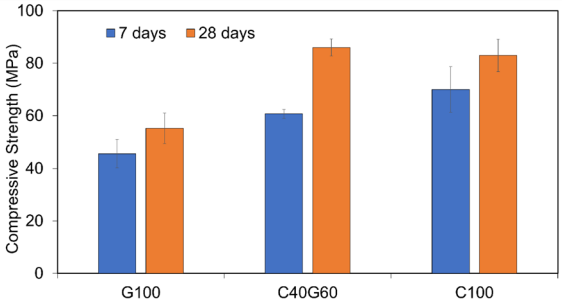

Fig. 13 Compressive strength of the binder.

since the adhesive properties signifies the ability of the fresh binder to stick with the coarse aggregate. Binder having higher adhesive force reflects to its greater ability to stick with the aggregates, resulting in the increase of compressive strength. Thus, it can be concluded that the adhesive properties of the GGBFS was found relatively weaker than OPC.

4.2 Compressive Strength

Fig. 12 compares the compressive strengths of the six concrete mixtures tested in this study; with two target porosities of 10% and 15% which consists of C100, C40G60 and G100. The compressive strengths at 28 days of curing range from approximately 13.3 to 24.9 MPa. The larger standard deviation observed in some of the samples were likely due to the nonuniformity compaction of the concrete. The compressive strength decreased as the GGBFS content increases at both 7 and 28 days. However, it is notable that the GGBFS only mixtures (G100P10, G100P15) exceed the minimum strength of pervious concrete required in most applications (ACI. 2010).

Fig. 12 also shows the relationship between the compressive strength and porosity of the concrete mixtures. Note that the measured porosity values are similar to the target porosity of 10% or 15%. In all binder cases, the P15 concrete mixture with a higher porosity had a lower compressive strength than P10 case at both 7 and 28 days. This was in accordance with findings in the literature (Kim et al., 2016; da Costa et al., 2021; Sun et al., 2018).

The rheological properties of fresh binders generally have a significant influence on the compressive strength of pervious concrete. As shown in Fig. 13, for target porosity of 15%, the C100 pervious concrete had a higher compressive strength than that of the C40G60 pervious concrete, despite the C40G60 binder having a higher compressive strength than the C100 binder, which is highly associated with the adhesive force. In addition, as for the C40G60, the adhesive characteristics are superior to G100, which explains why the pervious concrete made of C40G60 had a higher compressive strength than that made of G100. Therefore, it can be concluded that, as the amount of GGBFS increases, the adhesive properties of the binder decrease, causing a decrease in the compressive strength of the pervious concrete. The decrease in compressive strength of the G100 pervious concrete could be a result of the G100 binder imparting a higher plastic viscosity. Because the binder was unable to flow downward, the specimens were weaker at the bottom, which may have resulted in them breaking first.

4.3 Water Permeability

Water permeability experiments were carried out on the same three samples of each mix design which were subjected to the porosity test. The relationship between the permeability results assessed with the three methods and the measured porosity are displayed in Fig. 14. Regardless of the variability, when the measured porosity is high, the permeability increases, and when the measured porosity is low, the permeability decreases. EN 12697-19 (2012) comprises of two testing methods (i.e., vertical and horizontal). The vertical test method measures an almost similar trend of permeability results with ASTM and the falling head test method. However, the measured permeability results with the EN horizontal test method were much lower compared to the EN vertical test method, ASTM test method, and falling head test method because of the formula (Eq. 4) that is used to calculate the permeability, although the measured permeability correlates with the measured porosity. As for the EN horizontal, the equation does not consider the length of the specimen, since the water was allowed to permeate from the side of the specimen. Hence, it presents relatively lower water permeability results.

Higher permeability in the target porosity of 15% (P15) specimens with the falling head test method might be due to the turbulent flow of the water through

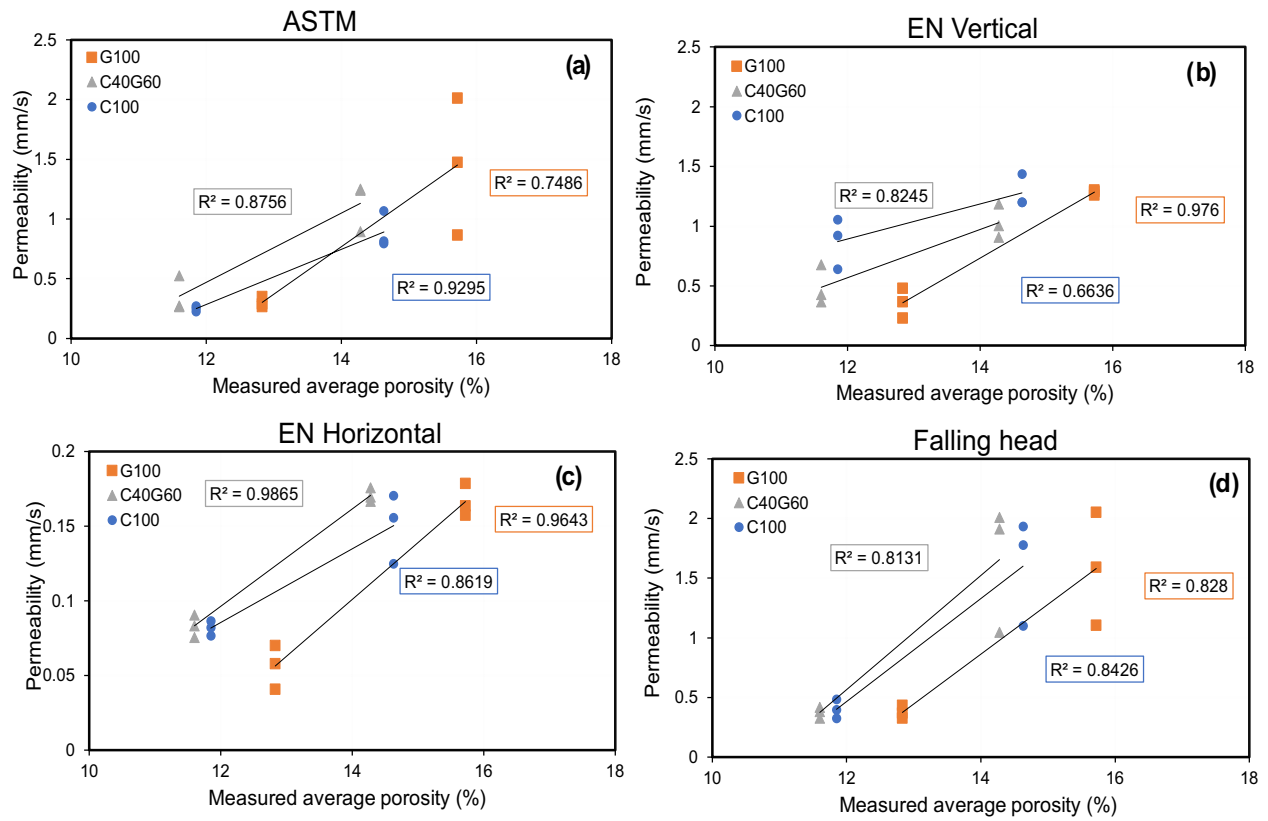

Fig. 14 Relationship between porosity and water permeability using various test methods: **a** ASTM; **b** EN vertical; **c** EN horizontal; and **d** falling head.

the specimens, the drop of water from a certain height can increase the tendency of the flow due to the presence of more voids thus increasing the velocity of the flow. In the constant head test, the flow of water follows the principle of laminar flow (Sandoval et al., 2017). However, the results obtained from the EN, falling head and ASTM test methods represented the same tendency as the measured porosity, showing a correlation between the two parameters.

Water permeability assessed using the EN vertical test method was inconsistent with measured porosity, with a poorer correlation coefficient for C100 than the other test methods. Significantly, the EN test method was used for higher porosity (20–30%) specimens and specified for bituminous mixtures with interconnecting voids (Lu et al., 2019). Meanwhile, the correlation between the measured permeabilities and porosities in the other test methodologies was almost equivalent. It was also possible to say that all the test methods are applicable and that a better test method for a sample with a low target porosity can be chosen.

4.4 Pore Structure Analysis Using Computer Tomography

A CT scan was conducted on to analyze the distribution of pores for a better understanding of water permeability. One sample out of the three samples used for porosity and permeability tests was used for each mixture. Fig. 15 shows the overall distribution of pores in the vertical direction of the pervious concretes. This figure represents a comparison of the distribution of pores for samples with assorted target porosities and binders. In the case of both the target porosities of C100 and C40G60, a higher porosity region was observed in the middle of the specimens. However, G100 showed a relatively uniform distribution of the pores compared to C100 and C40G60 in the top and middle portions of the specimen, although the distribution of pores increased around the bottom portion of the specimen. This might be due to less adhesive force between the binder and aggregate, causing the restriction of binder flowing down and resulting in less compressive strength. Moreover, larger amount of voids present at the bottom of the specimen might be also associated with the higher plastic viscosity.

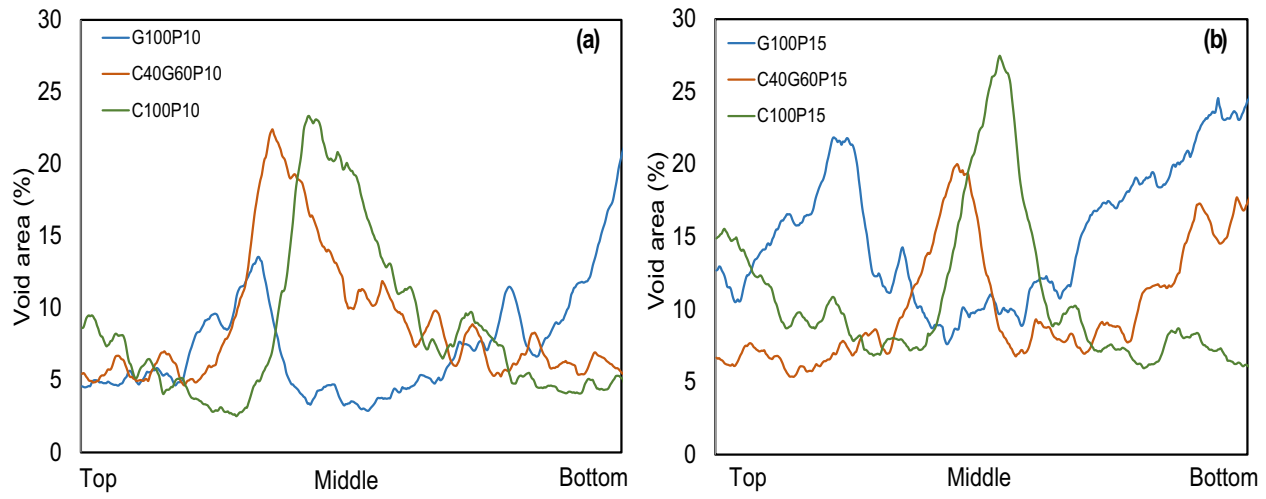

Fig. 15 Distribution of pores in the pervious concretes from CT images: **a** P10 samples; **b** P15 samples.

Among all the specimens, G100P10 had the lowest pore distribution on the middle portion, but the pores gradually increased with more pores at the bottom. Quite the contrary, C100P10 and C40G60P10 had a higher significant distribution of pores in the middle portion; however, the peak reduced with very low pore distribution at the bottom portion. Therefore, the distribution of pores was not uniform throughout for all the specimens, which may have been caused by factors, such as compaction force and the type of binders. The pervious concrete was hand compacted using a steel rod, which is a possible reason for the peak pore distribution at the middle and bottom portions (Alemu et al., 2021).

The comparison of the measured porosity between Archimedes' principle and a CT scan regarding the measured water permeability with various test methods is presented in Table 4. The findings verify that porosities using the CT scan were lower than those measured using Archimedes' principle. This might be due to the presence of aggregate in pervious concrete, which affects the factors of calculations of the pore area based on the color of the pixels and the detection of smaller pores in the CT scan test method (Alemu et al., 2021; Park et al., 2022). The measured water permeabilities and porosities obtained from the CT scan also have a strong relationship.

Among all the testing methods of water permeability, the ASTM and EN horizontal methods strongly demonstrate almost a similar correlation trend between the water permeabilities and porosities measured through CT scans for all the specimens. G100P15 had the highest CT scan-measured porosity of the pervious specimen, which reflects the highest water permeability presented with ASTM and EN vertical test methods. However, the overall water permeability obtained through ASTM and EN verticals does not exactly correlate with the porosity measured by the CT scan. While it is unsure if the porosity measured through a CT scan provides the actual skeleton porosity, it can be concluded that the ASTM test method best suits the

Table 4 Porosity results measured with the water absorption (Archimedes') method and CT scan and water permeability results.

Specimen	Target porosity (%)	Porosity (%)		Permeability (mm/s)			
		Archimedes'	CT Scan	ASTM	EN		Falling head
					EN vertical	EN horizontal	
G100	15	15.7	15.4	1.45	1.28	0.16	1.58
C40G60	15	14.2	10.4	1.12	1.03	0.17	1.65
C100	15	14.6	10.8	0.89	1.27	0.15	1.60
G100	10	12.1	7.6	0.30	0.35	0.05	0.37
C40G60	10	11.6	8.9	0.35	0.60	0.08	0.37
C100	10	11.84	8.5	0.25	0.87	0.08	0.40

correlation between water permeability and CT scan-measured porosity.

5 Conclusions

In this study, ground granulated blast furnace slag (GGBFS)-based pervious concrete was investigated. Two test variables were considered: OPC replacement ratio by GGBFS and target porosity, which was adjusted by the binder-to-aggregate ratio. Effects of the rheological properties of binders on the water permeability and compressive strength of pervious concretes were experimentally evaluated. CT scan test was also conducted to assess the influence of rheological properties and to enhance the comparison with the water permeability tests. The observations and findings of this study can be summarized as follows:

1. The plastic viscosity was the highest when only GGBFS was used as the binder, which might be due to the rough surface and structural breakdown of the binder during the test, since CaO is used as an activator and $CaCl_2$ as an accelerator. However, the yield stress of the OPC binder was higher than that of the GGBFS binder, which may be due to the stronger adhesive properties between the particles without paste segregation. When the adhesive force of the binder was lower, the CT scan revealed that pore distribution was higher at the bottom of the specimen which may be due to the restriction of flowing down of the binder at the bottom due to higher plastic viscosity of GGBFS.
2. As for the GGBFS-only case, the strength and flowability of the binder were not directly correlated with the strength of the associated pervious concrete. In relation to the amount of GGBFS, the adhesive force of the binder had the greatest impact on the compressive strength of the pervious concrete. As the amount of GGBFS increased, the adhesive force of the binder decreased, causing a decrease in the compressive strength of pervious concrete due to its poor ability to stick to coarse aggregates.
3. The porosity estimated by Archimedes' principle and CT scan was significantly related to the water permeability determined by all three techniques. Due to the reduced target porosities, there were no considerable discrepancies in the results of the three water permeability test techniques.
4. The pervious concrete manufactured with 60% GGBFS has nearly identical compressive strength, porosity, and permeability to the pervious concrete manufactured with OPC, which can minimize a significantly larger carbon footprint. However, the pervious concrete with CaO-activated GGBFS has a relatively lower compressive strength, since the adhesive force of the binder was relatively weaker compared to those with less GGBFS.

It is hoped that the results from this experimental research will provide basic information for developing GGBFS-based pervious concrete for sustainable pavement development. However, additional research is needed to improve the strength and pore distribution of CaO-activated GGBFS pervious concrete and assess the water permeability with a higher target porosity.

Acknowledgements
Not applicable.

Author Contributions
YO: conceptualization, methodology, investigation, validation, formal analysis, investigation, data curation, writing—original draft preparation, writing—review and editing, visualization; SJ: methodology, investigation, validation, formal analysis, data curation, writing—review and editing; SG: methodology, investigation, validation, formal analysis, data curation, writing—review and editing; MS: writing—review and editing, resources, supervision, project administration, funding acquisition; SP: writing—review and editing, resources, supervision, project administration, funding acquisition; All authors read and approved the final manuscript.

Authors' Information
YO is a Graduate student in the Department of Urban and Environmental Engineering at Ulsan National Institute of Science and Technology (UNIST), Ulsan, Republic of Korea. SJ is a Graduate student in the Department of Urban and Environmental Engineering at Ulsan National Institute of Science and Technology (UNIST), Ulsan, Republic of Korea. SG is a Postdoctoral Researcher in the Department of the Institute of Engineering Research at Seoul National University, Seoul, Republic of Korea. MS is a Full Professor in the Department of Urban and Environmental Engineering at Ulsan National Institute of Science and Technology (UNIST), Ulsan, Republic of Korea. SP is an Assistant Professor in the Department of Urban and Environmental Engineering at Ulsan National Institute of Science and Technology (UNIST), Ulsan, Republic of Korea.

Funding
This work was supported by the National Research Foundation of Korea (NRF) Grant funded by the Korea government (MSIT) (No. 2021R1A4A1030867 and 2021R1C1C1008671).

Availability of Data and Materials
The data and materials are included in the manuscript.

Declarations

Ethics Approval and Consent to Participate
Not applicable.

Consent for Publication
Not applicable.

Competing Interests
The authors declare no competing interest.

Author details
[1]Department of Urban and Environmental Engineering, Ulsan National Institute of Science and Technology (UNIST), 50 UNIST-gil, Ulsan 44919, Republic of Korea. [2]Institute of Engineering Research, Seoul National University, Seoul 08826, Republic of Korea.

Received: 29 March 2022 Accepted: 19 July 2022
Published online: 07 November 2022

References

ACI Committee 522, & American Concrete Institute. (2010). *Report on pervious concrete*. Farmington Hills: American Concrete Institute.

Alemu, A. S., Yoon, J., Tafesse, M., Seo, Y. S., Kim, H. K., & Pyo, S. (2021). Practical considerations of porosity, strength, and acoustic absorption of structural pervious concrete. *Case Studies in Construction Material*. https://doi.org/10.1016/j.cscm.2021.e00764

ASTM C1749 17A. 2012. https://doi.org/10.1520/c1749-17A

ASTM C1231. 2015. https://doi.org/10.1520/C1231_C1231M-15

ASTM C1701. 2017. https://doi.org/10.1520/C1701_C1701M-17A

ASTM C109. 2020. https://doi.org/10.1520/C0109_C0109M-21

ASTM C230. 2020. https://doi.org/10.1520/C0230_C0230M-21

Batezini, R., & Balbo, J. T. (2015). Study on the hydraulic conductivity by constant and falling head methods for pervious concrete. *Revista IBRACON De Estruturas e Materiais, 8*(3), 248–259. https://doi.org/10.1590/s1983-41952015000300002

Chandrappa, A. K., & Biligiri, K. P. (2016). Comprehensive investigation of permeability characteristics of pervious concrete: A hydrodynamic approach. *Construction and Building Materials, 123*, 627–637. https://doi.org/10.1016/j.conbuildmat.2016.07.035

Cui, X., Zhang, J., Huang, D., Liu, Z., Hou, F., Cui, S., Zhang, L., & Wang, Z. (2017). Experimental study on the relationship between permeability and strength of pervious concrete. *Journal of Materials in Civil Engineering, 29*(11), 04017217. https://doi.org/10.1061/(asce)mt.1943-5533.0002058

EN 12697-19 (2012). *Bituminous mixtures — Test methods for hot mix asphalt*. Part 19: Permeability of specimen. BSI Standards Publication, Brussels

Gołaszewski, J., & Szwabowski, J. (2004). Influence of superplasticizers on rheological behaviour of fresh cement mortars. *Cement and Concrete Research, 34*(2), 235–248. https://doi.org/10.1016/j.cemconres.2003.07.002

Gwon, S., & Shin, M. (2019). Rheological properties of modified sulfur polymer composites containing cement-fly ash blend at different temperatures. *Construction and Building Materials*. https://doi.org/10.1016/j.conbuildmat.2019.116784

Huang, B., Wu, H., Shu, X., & Burdette, E. G. (2010). Laboratory evaluation of permeability and strength of polymer-modified pervious concrete. *Construction and Building Materials, 24*(5), 818–823. https://doi.org/10.1016/j.conbuildmat.2009.10.025

Kim, H., Hong, J., & Pyo, S. (2018). Acoustic characteristics of sound absorbable high performance concrete. *Applied Acoustics, 138*, 171–178. https://doi.org/10.1016/j.apacoust.2018.04.002

Kim, H. H., Kim, C. S., Jeon, J. H., & Park, C. G. (2016). Effects on the physical and mechanical properties of porous concrete for plant growth of blast furnace slag, natural jute fiber, and styrene butadiene latex using a dry mixing manufacturing process. *Materials*. https://doi.org/10.3390/ma9020084

Kim, M. S., Jun, Y., Lee, C., & Oh, J. E. (2013). Use of CaO as an activator for producing a price-competitive non-cement structural binder using ground granulated blast furnace slag. *Cement and Concrete Research, 54*, 208–214. https://doi.org/10.1016/j.cemconres.2013.09.011

Lee, J. W., Jang il, Y., Park, W. S., & Kim, S. W. (2016). A study on mechanical properties of porous concrete using cementless binder. *International Journal of Concrete Structures and Materials, 10*(4), 527–537. https://doi.org/10.1007/s40069-016-0166-3

Lin, W., Park, D. G., Ryu, S. W., Lee, B. T., & Cho, Y. H. (2016). Development of permeability test method for porous concrete block pavement materials considering clogging. *Construction and Building Materials, 118*, 20–26. https://doi.org/10.1016/j.conbuildmat.2016.03.107

Liu, R., Chi, Y., Chen, S., Jiang, Q., Meng, X., Wu, K., & Li, S. (2020). Influence of pore structure characteristics on the mechanical and durability behavior of pervious concrete material based on image analysis. *International Journal of Concrete Structures and Materials*. https://doi.org/10.1186/s40069-020-00404-1

Lu, G., Renken, L., Li, T., Wang, D., Li, H., & Oeser, M. (2019). Experimental study on the polyurethane-bound pervious mixtures in the application of permeable pavements. *Construction and Building Materials, 202*, 838–850. https://doi.org/10.1016/j.conbuildmat.2019.01.051

Ma, S., Qian, Y., & Kawashima, S. (2018). Performance-based study on the rheological and hardened properties of blended cement mortars incorporating palygorskite clays and carbon nanotubes. *Construction and Building Materials*, *171*, 663–671. https://doi.org/10.1016/j.conbuildmat.2018.03.121

Meyer, C. (2009). The greening of the concrete industry. *Cement and Concrete Composites, 31*(8), 601–605. https://doi.org/10.1016/j.cemconcomp.2008.12.010

Naik, T. R. (2005). Sustainability of the cement and concrete industries. In R. K. Dhir, T. D. Dyer, & M. D. Newlands (Eds.), *Achieving Sustainability in Construction: Proceedings of the International Conference held at the University of Dundee, Scotland, UK on 5–6 July 2005*. London: Thomas Telford Publishing.

Palacios, M., Banfill, P. F. G., & Puertas, F. (2008). Rheology and setting of alkali-activated slag pastes and mortars effect of organic admixture. *ACI Materials Journal, 105*(2), 140.

Park, S., Ju, S., Kim, H. K., Seo, Y. S., & Pyo, S. (2022). Effect of the rheological properties of fresh binder on the compressive strength of pervious concrete. *Journal of Materials Research and Technology, 17*, 636–648. https://doi.org/10.1016/j.jmrt.2022.01.045

Peng, H., Yin, J., & Song, W. (2018). Mechanical and hydraulic behaviors of eco-friendly pervious concrete incorporating fly ash and blast furnace slag. *Applied Sciences (switzerland), 8*(6), 859. https://doi.org/10.3390/app8060859

Pereira da Costa, F. B., Haselbach, L. M., & da Silva Filho, L. C. P. (2021). Pervious concrete for desired porosity: Influence of w/c ratio and a rheology-modifying admixture. *Construction and Building Materials*. https://doi.org/10.1016/j.conbuildmat.2020.121084

Qin, Y., Yang, H., Deng, Z., & He, J. (2015). Water permeability of pervious concrete is dependent on the applied pressure and testing methods. *Advances in Materials Science and Engineering*. https://doi.org/10.1155/2015/404136

Saboo, N., Shivhare, S., Kori, K. K., & Chandrappa, A. K. (2019). Effect of fly ash and metakaolin on pervious concrete properties. *Construction and Building Materials, 223*, 322–328. https://doi.org/10.1016/j.conbuildmat.2019.06.185

Sandoval, G. F. B., Galobardes, I., Teixeira, R. S., & Toralles, B. M. (2017). Comparison between the falling head and the constant head permeability tests to assess the permeability coefficient of sustainable Pervious Concretes. *Case Studies in Construction Materials, 7*(September), 317–328. https://doi.org/10.1016/j.cscm.2017.09.001

Song, H. W., & Saraswathy, V. (2006). Studies on the corrosion resistance of reinforced steel in concrete with ground granulated blast-furnace slag—an overview. *In Journal of Hazardous Materials, 138*(2), 226–233. https://doi.org/10.1016/j.jhazmat.2006.07.022

Sriravindrarajah, R., Wang, N. D. H., & Ervin, L. J. W. (2012). Mix design for pervious recycled aggregate concrete. *International Journal of Concrete Structures and Materials, 6*(4), 239–246. https://doi.org/10.1007/s40069-012-0024-x

Sun, Z., Lin, X., & Vollpracht, A. (2018). Pervious concrete made of alkali activated slag and geopolymers. *Construction and Building Materials, 189*, 797–803. https://doi.org/10.1016/j.conbuildmat.2018.09.067

Thompson, R., Smith, R. B., Bou Karim, Y., Shen, C., Drummond, K., Teng, C., & Toledano, M. B. (2022). Noise pollution and human cognition: An updated systematic review and meta-analysis of recent evidence. *In Environment International*. https://doi.org/10.1016/j.envint.2021.106905

Wang, J., & Liu, E. (2020). Upcycling waste seashells with cement: Rheology and early-age properties of Portland cement paste. *Resources, Conservation and Recycling*. https://doi.org/10.1016/j.resconrec.2020.104680

Wang, J., Liu, E., & Li, L. (2018). Multiscale investigations on hydration mechanisms in seawater OPC paste. *Construction and Building Materials, 191*, 891–903. https://doi.org/10.1016/j.conbuildmat.2018.10.010

Wang, J., Xie, J., Wang, Y., Liu, Y., & Ding, Y. (2020). Rheological properties, compressive strength, hydration products and microstructure of seawater-mixed cement pastes. *Cement and Concrete Composites*. https://doi.org/10.1016/j.cemconcomp.2020.103770

Wang, Y., He, F., Wang, J., Wang, C., & Xiong, Z. (2019a). Effects of calcium bicarbonate on the properties of ordinary Portland cement paste. *Construction and Building Materials, 225*, 591–600. https://doi.org/10.1016/j.conbuildmat.2019.07.262

Wang, Y., Yu, J., Wang, J., & Guan, X. (2019b). Effects of aluminum sulfate and quicklime/fluorgypsum ratio on the properties of Calcium Sulfoaluminate (CSA) cement-based double liquid grouting materials. *Materials, 12*(8), 1222. https://doi.org/10.3390/ma12081222

Yao, X., Yu, K., Zeng, X., Lin, Y., Ye, B., Shen, X., & Liu, J. (2022). How can urban parks be planned to mitigate urban heat island effect in "Furnace cities"?

An accumulation perspective. *Journal of Cleaner Production*. https://doi.org/10.1016/j.jclepro.2021.129852

Yu, F., Sun, D., Wang, J., & Hu, M. (2019). Influence of aggregate size on compressive strength of pervious concrete. *Construction and Building Materials, 209*, 463–475. https://doi.org/10.1016/j.conbuildmat.2019.03.140

Yum, W. S., Jeong, Y., Yoon, S., Jeon, D., Jun, Y., & Oh, J. E. (2017). Effects of CaCl2 on hydration and properties of lime(CaO)-activated slag/fly ash binder. *Cement and Concrete Composites, 84*, 111–123. https://doi.org/10.1016/j.cemconcomp.2017.09.001

Yum, W. S., Suh il, J., Jeon, D., & Oh, J. E. (2020). Strength enhancement of CaO-activated slag system through addition of calcium formate as a new auxiliary activator. *Cement and Concrete Composites*. https://doi.org/10.1016/j.cemconcomp.2020.103572

Zhang, Q., Li, P., Lyu, Q., Ren, X., & He, S. (2022). Groundwater contamination risk assessment using a modified DRATICL model and pollution loading: A case study in the Guanzhong Basin of China. *Chemosphere*. https://doi.org/10.1016/j.chemosphere.2021.132695

Zhang, Y., Li, H., Abdelhady, A., & Yang, J. (2020). Comparative laboratory measurement of pervious concrete permeability using constant-head and falling-head permeameter methods. *Construction and Building Materials*. https://doi.org/10.1016/j.conbuildmat.2020.120614

Publisher's Note